



# The Disk Substructures at High Angular Resolution Project (DSHARP). X. Multiple Rings, a Misaligned Inner Disk, and a Bright Arc in the Disk around the T Tauri star HD 143006

Laura M. Pérez<sup>1</sup>, Myriam Benisty<sup>1,2,3</sup>, Sean M. Andrews<sup>4</sup>, Andrea Isella<sup>5</sup>, Cornelis P. Dullemond<sup>6</sup>, Jane Huang<sup>4</sup>, Nicolás T. Kurtovic<sup>1</sup>, Viviana V. Guzmán<sup>7,8</sup>, Zhaohuan Zhu<sup>9</sup>, Tilman Birnstiel<sup>10</sup>, Shangjia Zhang<sup>9</sup>, John M. Carpenter<sup>7</sup>, David J. Wilner<sup>4</sup>, Luca Ricci<sup>11</sup>, Xue-Ning Bai<sup>12</sup>, Erik Weaver<sup>5</sup>, and Karin I. Öberg<sup>4</sup>

<sup>1</sup> Departamento de Astronomía, Universidad de Chile, Camino El Observatorio 1515, Las Condes, Santiago, Chile; [lperez@das.uchile.cl](mailto:lperez@das.uchile.cl)

<sup>2</sup> Unidad Mixta Internacional Franco-Chilena de Astronomía, CNRS/INSU UMI 3386, France

<sup>3</sup> Univ. Grenoble Alpes, CNRS, IPAG, F-38000 Grenoble, France

<sup>4</sup> Harvard-Smithsonian Center for Astrophysics, 60 Garden Street, Cambridge, MA 02138, USA

<sup>5</sup> Department of Physics and Astronomy, Rice University 6100 Main Street, MS-108, Houston, TX 77005, USA

<sup>6</sup> Zentrum für Astronomie, Heidelberg University, Albert Ueberle Str. 2, D-69120 Heidelberg, Germany

<sup>7</sup> Joint ALMA Observatory, Avenida Alonso de Córdova 3107, Vitacura, Santiago, Chile

<sup>8</sup> Instituto de Astrofísica, Pontificia Universidad Católica de Chile, Av. Vicuña Mackenna 4860, 7820436 Macul, Santiago, Chile

<sup>9</sup> Department of Physics and Astronomy, University of Nevada, Las Vegas, 4505 South Maryland Parkway, Las Vegas, NV 89154, USA

<sup>10</sup> University Observatory, Faculty of Physics, Ludwig-Maximilians-Universität München, Scheinerstr. 1, D-81679 Munich, Germany

<sup>11</sup> Department of Physics and Astronomy, California State University Northridge, 18111 Nordhoff Street, Northridge, CA 91130, USA

<sup>12</sup> Institute for Advanced Study and Tsinghua Center for Astrophysics, Tsinghua University, Beijing 100084, People's Republic of China

Received 2018 October 8; revised 2018 November 21; accepted 2018 November 23; published 2018 December 26

## Abstract

We present a detailed analysis of new Atacama Large Millimeter/submillimeter Array (ALMA) observations of the disk around the T-Tauri star HD 143006, which at 46 mas (7.6 au) resolution reveals new substructures in the 1.25 mm continuum emission. The disk resolves into a series of concentric rings and gaps, together with a bright arc exterior to the rings that resembles hydrodynamical simulations of a vortex and a bridge-like feature connecting the two innermost rings. Although our <sup>12</sup>CO observations at similar spatial resolution do not show obvious substructure, they reveal an inner disk depleted of CO emission. From the continuum emission and the CO velocity field we find that the innermost ring has a higher inclination than the outermost rings and the arc. This is evidence for either a small ( $\sim 8^\circ$ ) or moderate ( $\sim 41^\circ$ ) misalignment between the inner and outer disk, depending on the specific orientation of the near/far sides of the inner/outer disk. We compare the observed substructures in the ALMA observations with recent scattered-light data of this object from the Very Large Telescope/Spectro-Polarimetric High-contrast Exoplanet REsearch (SPHERE). In particular, the location of narrow shadow lanes in the SPHERE image, combined with pressure-scale height estimates, favor a large misalignment of about  $41^\circ$ . We discuss our findings in the context of a dust-trapping vortex, planet-carved gaps, and a misaligned inner disk due to the presence of an inclined companion to HD 143006.

**Key words:** instrumentation: high angular resolution – instrumentation: interferometers – planet–disk interactions – protoplanetary disks – stars: individual (HD 143006)

## 1. Introduction

High-resolution observations of protoplanetary disks have shown that most, if not all, disks host substructures in the form of spiral arms, rings, or azimuthally asymmetric features. These features are imprints of the processes of disk evolution and planet formation, and can be observed from optical (in scattered light, e.g., Avenhaus et al. 2018) to millimeter wavelengths (e.g., Huang et al. 2018a, 2018b). In the dust continuum, the most common substructures are multiple bright rings and dark gaps, possibly tracing overdensities and depletion of dust grains, respectively. Rings and gaps are a natural outcome of dynamical interactions with planets (e.g., Paardekooper & Mellema 2004; Crida & Morbidelli 2007; Zhu et al. 2011), but could also be tracing ice lines (e.g., Zhang et al. 2015; Okuzumi et al. 2016) or be a result of certain magnetohydrodynamical processes (e.g., Johansen et al. 2009; Dittrich et al. 2013; Bai & Stone 2014; Simon & Armitage 2014; Béthune et al. 2017; Suriano et al. 2018).

These substructures could play a very important role in the process of planet formation, and in particular, in the first steps toward the growth of planetesimals. Alternatively, substructures

may exhibit the outcomes of planet–disk interactions, and serve as an important diagnostics of ongoing planet formation. Because dust particles experience aerodynamic drag from the gas, in a smooth disk they would rapidly lose angular momentum and drift toward the star before they can grow to planetesimal size (Brauer et al. 2007; Birnstiel et al. 2010). However, dust grains can be maintained in localized particle traps (pressure maxima) that allow them to efficiently grow (Pinilla et al. 2012a). Observationally, these traps appear as a suite of bright and dark rings in the dust continuum (Pinilla et al. 2012b) that are reminiscent of continuum observations of multiple ringed systems (e.g., ALMA Partnership et al. 2015). In addition to concentric rings, azimuthal asymmetries have also been observed, in particular in protoplanetary disks with dust-depleted large cavities (transition disks; e.g., Casassus et al. 2013; Isella et al. 2013; Dong et al. 2018). They are interpreted as azimuthal dust trapping (Birnstiel et al. 2013; Lyra & Lin 2013), possibly in a vortex due to the Rossby wave instability (e.g., Li et al. 2000; Meheut et al. 2012; Zhu & Stone 2014). Such an instability can be generated at the edge of a gap created by a massive planet (e.g., Regály et al. 2012; Ataiee et al. 2013;

Zhu & Baruteau 2016), or at the edge of a dead zone (e.g., Kretke & Lin 2007; Flock et al. 2017).

Planet–disk interactions can also leave imprints on the disk gas kinematics (Pérez et al. 2015), and observations of CO isotopologues have revealed non-Keplerian velocities in various disks. Recently, Pinte et al. (2018) found a local deformation of the CO disk velocity field of the intermediate-mass young star HD 163296, consistent with the spiral wave induced by a  $2 M_{\text{Jup}}$  planet located at 260 au. Teague et al. (2018) measured, in the same disk, local pressure gradients that are consistent with gaps carved by a  $1 M_{\text{Jup}}$  planet at 83 and 137 au. Other observations of non-Keplerian velocities were explained by the presence of radial flows (Rosenfeld et al. 2014), of a warp (Rosenfeld et al. 2012; Casassus et al. 2015; Walsh et al. 2017), or of free-falling gas connecting a strongly misaligned inner disk to the outer disk (Loomis et al. 2017). A misalignment between the inner and outer disk could be induced by a massive companion on an inclined orbit with respect to the plane of the disk (e.g., Bitsch et al. 2013; Owen & Lai 2017), or alternatively, by a misaligned stellar magnetic field (Bouvier et al. 2007), in which case the star should be periodically obscured (periodic dippers; see e.g., Cody et al. 2014). In the presence of a strongly misaligned inner disk, the outer disk illumination is drastically affected, as evidenced by shadows observed in scattered-light images that trace the surface of the disk (e.g., Marino et al. 2015; Benisty et al. 2017, 2018; Casassus et al. 2018; Pinilla et al. 2018).

The focus of this Letter is the T-Tauri star HD 143006, a G-type star ( $1.8^{+0.2}_{-0.3} M_{\odot}$ , 4–12 Myr old; Preibisch et al. 2002; Pecaute et al. 2012; Andrews et al. 2018; Garufi et al. 2018), located in Upper Sco at a distance of  $165 \pm 5$  pc (Gaia Collaboration et al. 2018). Submillimeter continuum observations of the disk at moderate spatial resolution revealed an azimuthal asymmetry and a marginally resolved cavity (Barenfeld et al. 2016), although it is not classified as a transition disk from its spectral energy distribution. A strong near-infrared excess and typical mass accretion rate ( $\sim 2 \times 10^{-8} M_{\odot} \text{ yr}^{-1}$ ; Rigliaco et al. 2015) indicate that the innermost regions retain dust and gas. Recent scattered-light observations of HD 143006 show multiple brightness asymmetries: a shadow over half of the disk (the west side) and two additional narrow shadow lanes, both suggestive of a moderately misaligned inner disk (Benisty et al. 2018, and Section 4.2).

In the following, we present new observations of HD 143006 obtained with the Atacama Large Millimeter/submillimeter Array (ALMA) as part of the Disk Substructures at High Angular Resolution Project (DSHARP) in Section 2. We then present a characterization of its substructures in Section 3, which we further discuss in Section 4, and we present the conclusions of our work in Section 5.

## 2. Observations

Dust-continuum emission at 1.25 mm and  $^{12}\text{CO}$  emission in the  $J = 2-1$  transition were observed with long and short baselines in the ALMA Large Program 2016.1.00484.L. Additional short-baseline observations (from project 2015.1.00964.S, PI: K. I. Öberg) in the same dust and gas tracers were combined to increase  $uv$ -coverage on the short spacings. Details on the calibration of visibilities can be found in Andrews et al. (2018). Observations were centered to R.A. (J2000) =  $15^{\text{h}} 58^{\text{m}} 36^{\text{s}}.90$ , decl. (J2000) =  $-22^{\circ} 57' 15''.603$ , which are the coordinates of the phase center of the last

execution of the long-baseline observations. The continuum images presented here used the same imaging parameters as listed in Table 4 of Andrews et al. (2018), while the CO images were obtained using a robust parameter of 0.8 with a  $uv$ -tapering of 20 mas, which was applied to the CO visibilities to enhance extended emission from the disk. The rms noise in the continuum image is  $14.3 \mu\text{Jy beam}^{-1}$  for a 46–45 mas beam with position angle (PA) of  $52^{\circ}.1$ . In the CO spectral cube we measured an rms noise of  $1.04 \text{ mJy beam}^{-1} \text{ km s}^{-1}$ , for a beam size of  $66 \times 49$  mas, PA of  $83^{\circ}.6$ , and channel width of  $0.32 \text{ km s}^{-1}$ . The continuum map is presented in Figure 1, and the full set of CO channel maps in Figure 5.9 of Andrews et al. (2018).

## 3. Results

### 3.1. Dust Continuum Emission

The continuum emission from HD 143006, presented in Figure 1, is observed close to face-on: the disk resolves into an inner depleted region, three bright rings at roughly  $0''.05$  (8 au),  $0''.24$  (40 au), and  $0''.39$  (64 au) from the disk center, two dark annuli at roughly  $0''.13$  (22 au) and  $0''.31$  (51 au), and a bright southeast asymmetric feature just outside of the outermost ring at  $0''.45$  (74 au) from the disk center. This prominent arc is located at a PA (defined from the north toward the east) of  $\sim 140^{\circ}$  and has an azimuthal extent of  $\sim 30^{\circ}$ . From now on, we follow the convention of Huang et al. (2018a) and label the dark/bright annular features with a letter “D”/“B” followed by their radial location in au. Then, the innermost bright ring is labeled B8, the second bright ring as B40 and the outermost bright ring as B64. The dark annuli between B8 and B40, and between B40 and B64 are labeled D22 and D51, respectively.

The radial profile of the continuum emission presented in Huang et al. (2018a) indicates that B8 and B40 have a contrast of  $\sim 42$  and  $\sim 24$  with respect to the D22; these are one of the highest-contrast ring-features of the DSHARP sample. However, these rings are not completely smooth: B8 has two peaks along a PA of  $\sim 165^{\circ}$  (see panel (a) on Figure 1), but this is due to its inclination w.r.t. our line of sight (see Section 3.4). The outermost rings, B40 and B64, both peak close to a PA of  $180^{\circ}$  (better seen in the residual maps of Section 3.4). The bright asymmetric feature outside of B64 (see panel (b) on Figure 1) is also uneven in the azimuthal direction: the arc resolves into three peaks along its azimuthal extent. The brightest peak at the center of the arc has a signal-to-noise ratio (S/N) of 48, while the flanking peaks have a S/N of 44 and are separated by  $\sim 10$  au (60 mas) from the brightest peak of the arc. Finally, the dark annuli are not completely empty, in particular, inside D22 there is a bridge-like emission feature, with a S/N of  $4.9\sigma$ , connecting the B8 and B40 rings (see emission between the rings at a PA of  $\sim 300^{\circ}$  in panel (a) of Figure 1).

### 3.2. Gas Emission Traced by CO

The overall emission from the gaseous component of the HD 143006 disk, as traced by the CO line, is presented in the middle and right panels of Figure 2 and extends out to  $\sim 1''$  in radius, twice larger in radial extent than the dust continuum emission. CO emission is detected above  $3\sigma$  from  $-0.12$  to  $15.2 \text{ km s}^{-1}$  in the LSRK reference frame, with a systemic velocity of  $\sim 7.7 \text{ km s}^{-1}$ . The integrated intensity of CO, also known as moment 0 map (left panel, Figure 2) is not centrally peaked. Because the continuum emission appears to be

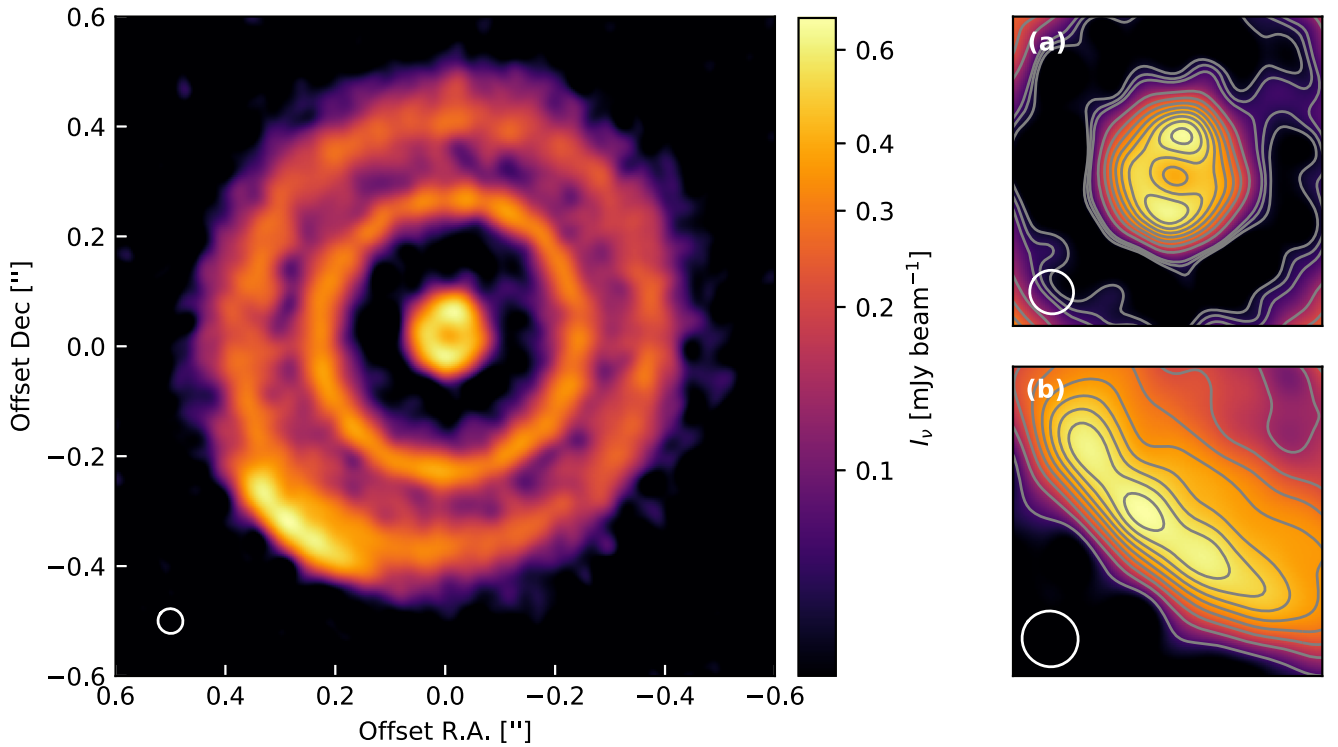


**Figure 1.** Left panel: ALMA observations at 1.25 mm of the dust-continuum emission from the disk around the young star HD 143006. The right panels show a zoom to (a) the inner disk within  $0.32''$ , and (b) the arc substructure within  $0.25''$ . In panel (a), the contours start at 3, 4,  $5\sigma$ , then are spaced by  $5\sigma$ , while in panel (b) contours start and are spaced by  $5\sigma$ , where  $\sigma$  is the rms noise of the image ( $\sigma = 14.3 \mu\text{Jy beam}^{-1}$ ). Ellipses in the bottom-left corner of each panel indicate the beam size of  $46 \times 45 \text{ mas}$  ( $7.6 \times 7.4 \text{ au}$ ).

optically thin ( $\tau < 0.2$ , Huang et al. 2018a), the lack of CO emission in the inner disk cannot be fully explained by continuum subtraction of optically thick dust emission, and rather indicates that some gas depletion occurs in the inner disk.

The intensity-weighted velocity of CO, also known as moment 1 map (right panel, Figure 2), shows a clear rotation pattern for a nearly face-on disk with a PA of  $\sim 165^\circ$  (note that the moment 0 map has two maxima along a similar PA). However, the disk rotation is not perfectly described by a single geometry, as can be seen on the inset of Figure 2, right panel, where the velocity field in the inner disk appears different from the outer disk. This difference will be quantified in the next sections.

Given the low inclination of this system and the low S/N of the spectral cube (peak S/N of  $\sim 11$ ), the front and back sides of the CO-emitting layers are not clearly separated, a feature observed in other disks with higher line-of-sight inclinations (e.g., Rosenfeld et al. 2013; Isella et al. 2018). Nevertheless, of the two possibilities for the absolute disk geometry, we suggest that the west side of the disk is the one closest to us: at every channel, the west side of the disk appears shorter when projected onto the rotation axis of the disk than the east side (see Figure 5.9 in Andrews et al. 2018).

Finally, a close inspection of the channel maps revealed that redshifted emission close to the systemic velocity has a deviation or “kink” from the Keplerian isovelocity curves that is not present in the blueshifted channels. This kink is marked by an arrow on the bottom panels (redshifted channels) of Figure 7 (see Appendix) and appears at a PA of between  $\sim 80^\circ$ – $120^\circ$ .

### 3.3. Modeling CO Kinematics

We model the Keplerian velocity field in HD 143006 using an analytical model of a razor-thin disk in Keplerian motion around a  $1.8 M_\odot$  star, in order to constrain the *global* geometry of the disk. The model parameters are the inclination ( $i$ ), PA, systemic velocity ( $v_{\text{sys}}$ ), as well as the R.A. and decl. offsets ( $x_0, y_0$ ) for the center of rotation. We fix the inner and outer radius of the disk to 0.3 and 250 au, respectively. For a given set of parameters we generate a velocity map that is convolved with the beam of our CO observations, which we then compare to the intensity-weighted velocity of CO (right panel of Figure 2) pixel by pixel. We perform our fit using an affine invariant MCMC sampler (*emcee*; Foreman-Mackey et al. 2013), and sample the parameters with uniform priors in the following range:  $i$  between  $[0^\circ, 90^\circ]$ , PA between  $[0^\circ, 360^\circ]$ ,  $v_{\text{sys}}$  between  $[5 \text{ km s}^{-1}, 10 \text{ km s}^{-1}]$ , and  $x_0, y_0$  between  $[-0.2'', 0.2'']$ . The parameter space is explored with 80 walkers and for 4000 steps. From the last 2000 steps we compute the best-fit values, which correspond to the 50th percentile of the samples in the marginalized distributions, while the error bars correspond to the 16th and 84th percentiles. The best-fit parameters can be found on Table 1, while Figure 3 presents the velocity field of the observations, best-fit model, and residual (computed by subtracting the model from the observations). Although the best-fit model reproduces the velocity field of the outer disk, inward of  $\sim 0.15''$  there are significant residuals that suggest gas moving at higher speeds than those in the model.

Note that if we separately fit the inner and outer disk kinematics, by masking the velocity field in Figure 3 inside and outside of  $0.15''$  (which corresponds to the midpoint separation



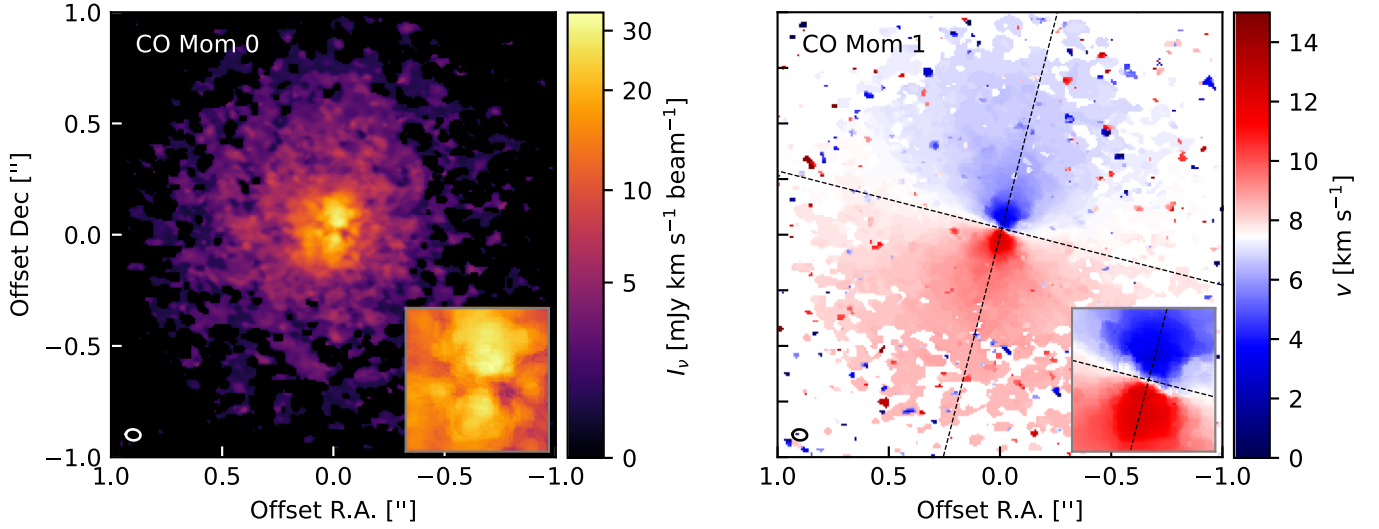


**Figure 2.** ALMA observations of the  $^{12}\text{CO}(J = 2 - 1)$  line from the disk around the young star HD 143006. Note that the field of view is  $2'' \times 2''$ , which is larger than in Figure 1. Left panel: map of the integrated intensity of the CO line. Right panel: map of the intensity-weighted velocity of the CO line. Insets on each panel show a zoom to the inner disk region within  $0.25''$ . The *global* PA of the disk, as constrained by the best-fit model in Section 3.3 to be  $167^\circ$ , is indicated by dashed lines. Ellipses on the bottom-left corner of each panel indicate beam size of  $66 \times 49$  mas ( $10.9 \times 8.1$  au).

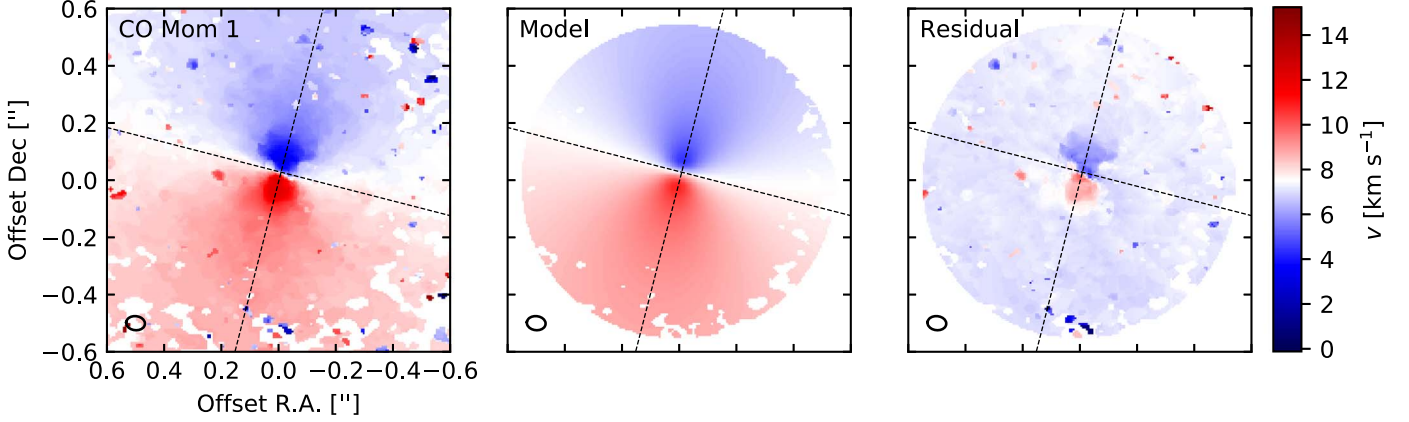


**Figure 3.** Comparison between the intensity-weighted velocity field around HD 143006 (left panel), the best-fit model for a Keplerian razor-thin disk (middle panel), and the residual velocity field map obtained from subtracting the best-fit from the observations (right panel). The *global* PA of the disk, as constrained by the best-fit model to be  $167^\circ$ , is indicated by dashed lines.

**Table 1**

Best-fit Model to the Intensity-weighted Velocity Field around HD 143006

Parameter		Best-fit Value
$x_0$	(mas)	$-6 \pm 3$
$y_0$	(mas)	$29 \pm 2$
$i$	( $^\circ$ )	$16.2 \pm 0.3$
PA	( $^\circ$ )	$167^\circ \pm 1^\circ$
$v_{\text{sys}}$	$\text{km s}^{-1}$	$7.71 \pm 0.02$

between B8 and B40), we find two different disk geometries. First, a fit for the geometry of the outer disk while excluding the inner disk (i.e., masking those pixels inside of  $0.15''$ ), results in a PA that is consistent with the global fit in Table 1 but a slightly more face-on outer disk with an inclination of  $14.59 \pm 0.02^\circ$ . On the other hand, when we only fit for the disk kinematics inside of  $0.15''$  (i.e., masking those pixels outside of  $0.15''$ ), we find  $i = 22.84 \pm 0.05^\circ$  and  $\text{PA} = 165.6 \pm 0.1^\circ$  for the inner disk. Thus, we constrain a difference between the inner and outer disk geometry, in particular, the inclination of

the disk changes from the inner to the outer disk (see Figure 8 in the Appendix for the best-fit model and residuals when the inner or outer disk are masked).

### 3.4. Modeling of Continuum Emission

To constrain the observed substructure in this disk, we generate simple morphological models that describe the emission for the observed rings and the southeast arc. These models are constructed by combining the emission of three radially Gaussian rings (that describe the B8, B40, and B64 features) and a 2D Gaussian, in both the radial and azimuthal direction (that describes the outermost arc feature).

For every ring, its intensity is given by

$$I(r) = I_R e^{-(r-r_R)^2/2\sigma_R^2}, \quad (1)$$

where  $I_R$  is the peak intensity at radius  $r_R$ ,  $\sigma_R$  is the ring width, and the ring is assumed to be symmetric along the azimuthal direction. For the asymmetric arc feature, its intensity is given

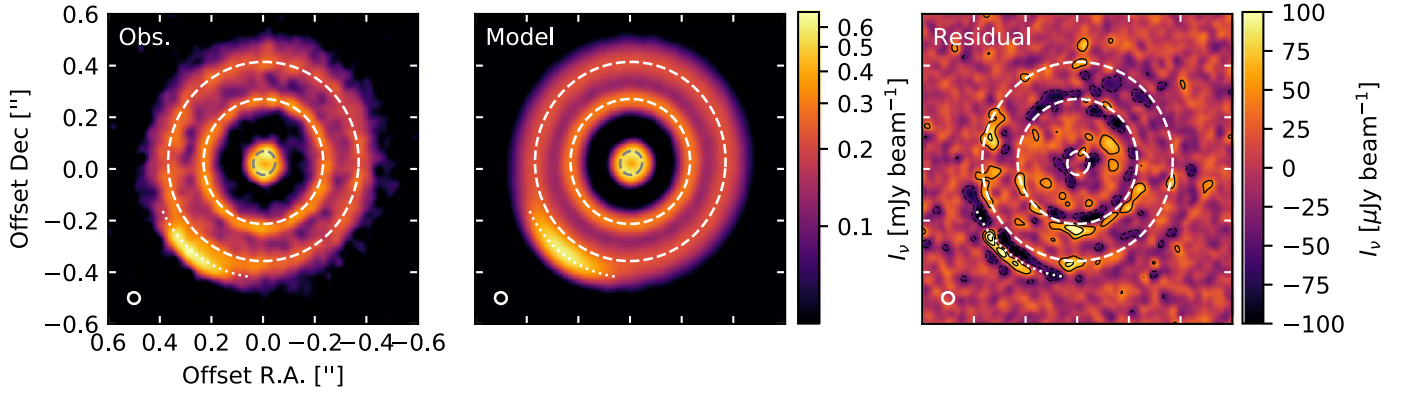


**Figure 4.** Comparison between the 1.25 mm observations from HD 143006 (left panel) with the image from the best-fit rings+arc morphological model (middle panel) and the residual map from subtracting the best-fit model from the observations (right panel). The location and geometry of the features, as constrained by the best-fit model, are indicated by dashed lines for B8, B40, and B64, and a dotted line for the arc. Ellipses on the bottom-left corner of each panel indicate the beam size, contours on the residual map start at  $3\sigma$  and are spaced by  $\pm 3\sigma$ , where  $\sigma$  is the rms noise of the dust continuum image.

**Table 2**  
Best-fit Model to the Dust Continuum Emission in HD 143006

Disk Geometry		Inner Disk		Outer Disk	
$i$	( $^\circ$ )	$24.1 \pm 1.0$		$17.02 \pm 0.14$	
PA	( $^\circ$ )	$164.3 \pm 2.4$		$176.2 \pm 0.6$	
$x_0$	(mas)	$-4.4 \pm 0.2$		$-1.0 \pm 0.2$	
$y_0$	(mas)	$23.1 \pm 0.2$		$28.9 \pm 0.2$	
Ring or Arc Parameters		B8	B40	B64	Arc
$I_R$ or $I_A$	( $\mu$ Jy)	$1.54 \pm 0.02$	$0.64 \pm 0.01$	$0.410 \pm 0.001$	$1.09 \pm 0.01$
$r_R$ or $r_A$	(au)	$7.67 \pm 0.04$	$39.95 \pm 0.03$	$63.6 \pm 0.1$	$74.2 \pm 0.1$
$\sigma_R$ or $\sigma_{r,A}$	(au)	$2.54 \pm 0.04$	$4.2 \pm 0.1$	$9.4 \pm 0.1$	$4.6 \pm 0.1$
$\sigma_{\theta,A}$	(au)	...	...	...	$21.1 \pm 0.1$
$\theta_A$	( $^\circ$ )	...	...	...	$141.4 \pm 0.1$

by

$$I(r, \theta) = I_A e^{-(r-r_A)^2/2\sigma_{r,A}^2} e^{-(\theta-\theta_A)^2/2\sigma_{\theta,A}^2}, \quad (2)$$

where  $I_A$  is the peak intensity at radius  $r_A$  and azimuthal location  $\theta_A$ , and  $\sigma_{r,A}$ ,  $\sigma_{\theta,A}$  are the width of the 2D Gaussian in the radial and azimuthal direction, respectively. The model adopted for the arc corresponds to the distribution of material in a steady-state vortex (Lyra & Lin 2013).

Additional parameters of importance are any offset ( $x_0$ ,  $y_0$ ) that the rings may have from the phase center of the observations defined in Section 2, and the inclination ( $i$ ) of each feature along a particular PA on the sky. Given the evidence for a misalignment between the inner disk and outer disk presented in Benisty et al. (2018), as well as the evidence from modeling its velocity field (Section 3.3), we assume that the features found in the outer disk (i.e., B40, B64, and the arc) share the same center, inclination, and PA, while the innermost ring (B8) may have a different geometry due to the misalignment (i.e., different center, inclination, and PA). This results in a total of 22 free parameters that are constrained with over 34 million visibilities. For a given set of parameters we produce a model image of the disk that is Fourier-transformed and sampled at the same locations in the  $uv$ -plane as the observed visibilities; for this we use the publicly available code Galario (Tazzari et al. 2018). To sample the probability density function (PDF) of our model parameters, we use the MCMC sampler *emcee* (Foreman-Mackey et al. 2013) with 120 walkers that we ran for 25,000 steps. Convergence was checked

by measuring the autocorrelation time, which was under 3000 iterations. For each parameter we compute the posterior PDF by marginalizing over all but the parameter of interest over the last 15,000 steps.

The best-fit values of the continuum emission model, chosen as the 50th percentile of the PDF, as well as the  $1\sigma$  uncertainty of each parameter from the 16th and 84th percentile of the PDF, are shown in Table 2. From the best fit we construct model visibilities (sampled at the same locations in  $uv$ -space as the observed visibilities) and we compute residual visibilities by subtracting the model visibilities from the observations. Images of the best-fit model and residual, obtained with the same imaging parameters as the observations (see Section 2), are presented in Figure 4.

The morphological models employed here can reproduce the observed emission reasonably well, as can be seen in the residual map of Figure 4 where leftover emission is minimal and the largest residual is at  $\pm 9\sigma$ . Huang et al. (2018a) find the rings locations directly on the image, resulting in differences of only 2%–3% for the outermost well-resolved rings and a 30% difference in the radial location of B8, which due to its small angular size will have much less independent measurements on the image. The radial width of the rings increases as a function of distance from the star: our model constrains radial extents of 6, 10, and 22 au (in FWHM) for B8, B40, and B64. When fitting width of each ring directly on the image, Dullemond et al. (2018) find a similar but narrower ring widths for B40 and B64, 7% and 30% narrower, respectively.

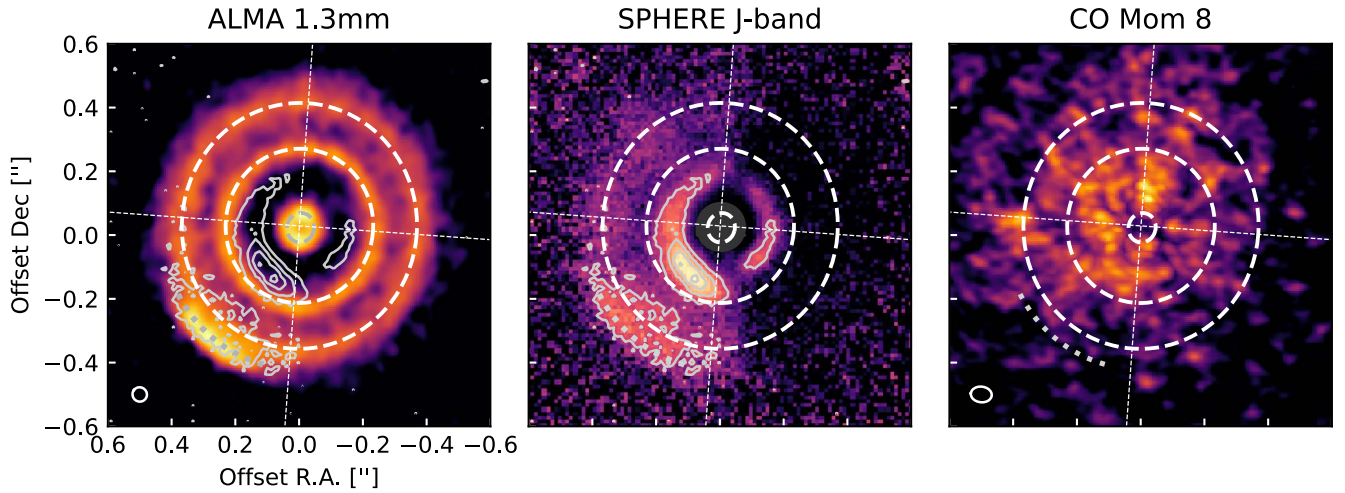


**Figure 5.** Comparison between the ALMA continuum emission (left panel), the Spectro-Polarimetric High-contrast Exoplanet REsearch (SPHERE) polarized intensity  $J$ -band observations (middle panel) and the  $^{12}\text{CO}$  peak emission map (right panel, also known as the moment 8 map). The thin dashed lines go along and perpendicular to the PA of the outer disk, while the location and geometry of the features, as constrained by the best-fit model, are indicated by dashed lines for B8, B40, and B64, and a dotted line for the arc. Contours are drawn at 25%, 50%, 75%, and 95% of the peak value of the SPHERE image in the middle panel. Ellipses on the bottom-left corner indicate the beam size for the ALMA observations.

As the rings are not completely symmetric in the azimuthal direction, for both B40 and B64 the radially Gaussian rings cannot reproduce the excess of emission seen in the south of each ring. For the southeast arc, our model constrains a narrow extent in the radial direction with a factor of  $\sim 4$  wider extent in the azimuthal direction, which is similar to that observed in other disks with arcs observed at lower angular resolution (e.g., Pérez et al. 2014). There are significant residuals at the arc location; in particular, the 2D-Gaussian prescription cannot properly describe the multiple peaks observed along the arc (Figure 1, panel (b)), which appear also in the residual map at the  $\sim 6\text{--}9\sigma$  level.

## 4. Discussion

### 4.1. Substructures in the ALMA Images

The distribution of larger solids, as traced by the ALMA dust continuum observations, reveals a wealth of substructure in the HD 143006 disk (Section 3.4), while the distribution of CO emission exhibits little substructure (only in the innermost disk regions, Section 3.3). This difference may arise from the fact that the 1.25 mm dust emission is optically thin throughout the disk (Huang et al. 2018a), while the observed CO emission is optically thick and traces the surface layers of the disk.

**Bright rings and dark annuli.** For the dark annuli D22 and D51, there is not a corresponding decrement of CO emission in either the channel maps (Figure 5.9 in Andrews et al. 2018) or the integrated CO emission map (Figure 2, right panel). Assuming that the dust depletion observed in the outermost dark annulus originates from dynamical clearing by objects embedded in the disk, Zhang et al. (2018) infer masses of  $\sim 10\text{--}20 M_{\text{Jup}}$  and  $\sim 0.2\text{--}0.3 M_{\text{Jup}}$ , for planets inside D22 and D51, respectively.

On the other hand, there is a decrement of both CO and dust emission inside B8. In particular, CO emission does not appear to be centrally peaked, either on the integrated emission map (moment 0 map, left panel of Figure 2) or in the peak emission map (moment 8 map, right panel of Figure 5). Although both these maps are susceptible to beam dilution effects (Weaver et al. 2018), which may cause an “false” inner cavity in the gas,

the lack of CO emission inside B8 is also observed in the channel maps away from the systemic velocity (see Appendix Figure 7, and Figure 5.9 in Andrews et al. 2018), meaning that there is some depletion of the CO column density inside of  $\sim 15$  au ( $\sim 90$  mas). We note that the lack of gas emission inside B8 cannot be explained by absorption from optically thick dust in the inner disk, as we also observe a dust emission deficit inside B8 and the emission from dust is optically thin throughout (Huang et al. 2018a). Most likely, the depletion of CO inside B8 is quite large; for example, in transition disk cavities with centrally peaked CO emission, the depletion has been measured to be more than an order of magnitude (van der Marel et al. 2015), and in the case of HD 143006 we do not observe a centrally peaked CO.

A possible origin for the depleted inner disk is photo-evaporation; however, the star is accreting at a moderate rate ( $2 \times 10^{-8} M_{\odot} \text{ yr}^{-1}$ ; Rigliaco et al. 2015) and the near-infrared excess points to a dust-rich inner disk, making this possibility less likely. A perturber inside B8 could deplete both gas and dust, and even misalign the inner disk, a possibility that will be discussed in Section 4.3.

**Bright arc in the southeast.** Vortices are regions of higher gas pressure that can very efficiently trap solids (e.g., Barge & Sommeria 1995; Klahr & Henning 1997; Baruteau & Zhu 2016). We model the arc emission with a prescription for the distribution of dust in a vortex that has reached steady state (Lyra & Lin 2013), and which should be smooth in the radial and azimuthal direction. However, the prominent arc in the 1.25 mm continuum images has further substructure: three separate peaks that are unresolved in the radial direction (see residual map in Figure 4), with a separation of  $\sim 10$  au from the central peak. During their lifetime, vortices may never reach a stable equilibrium. For example, simulations have shown that when the back-reaction of the dust onto the gas is taken into account, vortices may trap particles not in a single but in multiple structures, and it is this dust feedback that would eventually lead to the destruction of the vortex (see, e.g., Fu et al. 2014). Thus, it is not surprising that the observed arc has internal substructure.



The radial and azimuthal extent of the arc constrained by our model is about 5 by 21 au. From the midplane temperature profile ( $T_{\text{mid}}$ ) assumed in Huang et al. (2018a), we estimate that at the vortex location ( $\sim 74$  au), the pressure scale height corresponds to  $H_p \sim 5$  au (assuming a local sound speed of  $c_s = (k_B T_{\text{mid}} / \mu m_p)^{0.5}$ , and  $\mu = 2.3$ ). Thus, the vortex is radially as wide as  $H_p$  and it extends azimuthally over a few pressure scale heights, still consistent with the vortex scenario. In particular, the  $\sim 21$  au azimuthal extent is consistent with that of vortices formed at the edge of a gap/cavity, as it has a much smaller width than the  $\pi$ -wide vortices expected due to instabilities at the dead zone (Regály et al. 2017). However, the arc is outside of the millimeter dust disk, rather than at the edge of a dark annulus, and it is radially separated from B64 by  $\sim 10$  au. Such a configuration is similar to that of the disk in HD 135344B, which resolves into a narrow ring with an asymmetric arc outside of the ring (Cazzoletti et al. 2018). Simulations by Lobo Gomes et al. (2015) show that after a vortex forms at the edge of a planet-induced gap, the surface density can be enhanced further out in the disk than at the initial vortex location. Such density enhancement triggers again the Rossby wave instability and a second-generation vortex may form beyond the primary, leaving only the outermost vortex once the first one is damped. Thus, a second-generation vortex may explain the location of the observed arc in the outer disk of HD 143006.

We note that the vortex-like structure is not associated to spiral arms in scattered light (Benisty et al. 2018), unlike the well-studied cases of MWC 758 (Dong et al. 2018), HD 142527 (Avenhaus et al. 2014), and HD 135344B (Stolker et al. 2016), which in addition are classified as transition disks from their spectral energy distribution and whose central stars are Herbig ABe objects.

#### 4.2. Substructures Seen in Scattered Light

Figure 5 presents our continuum image (left panel), the polarized scattered light coronagraphic image of HD 143006 obtained with Very Large Telescope (VLT)/Spectro-Polarimetric High-contrast Exoplanet REsearch (SPHERE;<sup>13</sup> middle panel), and the peak intensity of the CO line at each velocity, also known as moment 8 map (right panel). The scattered-light image is a good tracer of small micron-sized dust grains located in tenuous disk surface layers, while the ALMA continuum image traces the millimeter-sized dust grains at the midplane. The peak intensity of the (optically thick) gas emission from CO (moment 8 image) also traces the upper disk layers.

Each pixel of the scattered-light image (middle panel, Figure 5) was scaled by  $r^2$ , where  $r$  is the distance to the central star, to compensate for the drop off in stellar illumination and allow a better detection of faint outer disk features. In this image, a broad shadow in the west, covering half of the disk, is present. In addition, the SPHERE image shows from inside out: a gap/cavity beyond the coronagraph radius ( $\sim 80$  mas, 13 au), a non-symmetric ring with two narrow shadow lanes aligned along the north–south direction, a gap not completely devoid of emission, and a non-symmetric outer disk. Both the outer disk and the inner ring present an overbrightness

along a small range of PAs ( $\sim 100^\circ$ – $170^\circ$ ; see contours in Figure 5).

##### 4.2.1. Comparison with CO Emission

As the CO line is optically thick, its intensity probes the temperature of the emitting gas, which, in turn depends on the amount of starlight received at the disk surface. In scattered light, the outer part of the disk is not detected in the west, indicating a drop of irradiation. To first approximation, the temperature of the CO-emitting layer should scale as the received luminosity to the one-fourth power, thus, we should also expect an east–west brightness asymmetry in the peak intensity CO map (left panel, Figure 5). We measure a east–west contrast in the CO peak intensity map of roughly  $\sim 1.2$ . The difference between the level of asymmetry in the scattered-light image and in the moment 8 map is likely related to the different depths of the  $\tau \sim 1$  layers in the two tracers. We note, however, that no substructure in the CO channel maps or moment maps is found to coincide with the narrow shadow lanes in the inner ring of the scattered light image.

The absence of an overbrightness in the CO peak intensity map at the location of the millimeter arc suggests that the overbrightness observed in scattered light does not only originate from an effect of a stronger irradiation. In addition, because the continuum emission in the arc is not optically thick ( $\tau \sim 0.4$  at the peak), this is unlikely to be an issue of continuum subtraction of optically thick emission on the CO line. As the inner disk is not probed by the SPHERE data, we cannot further compare the observed depletion of the CO column density inside of  $\sim 15$  au ( $\sim 90$  mas) discussed in Section 4.1. Interestingly, the “kink” seen in the channel maps (Section 3.2, also see Figure 7 in the Appendix) roughly coincides in radius and azimuthal extent with the overbrightness seen in scattered light along the inner ring.

##### 4.2.2. Comparison with Dust Continuum

The comparison between the ALMA continuum and the SPHERE scattered-light images indicates striking differences. Apart from the bright prominent arc in the outer disk, none of the features appear co-radial and none of the azimuthal asymmetries seen in scattered light have counterparts in the continuum image. Such differences are expected, as the two images trace distinct layers of the disk and different dust particles. The scattered-light image shows the regions of the disk that are directly lit by the star, and its appearance strongly depends on the shape of the disk surface, while the 1.25 mm continuum image shows the midplane features, whose brightness depend on the dust density, temperature, and opacity. A schematic of the features observed in the HD 143006 disk is presented in Figure 6 and will be discussed here.

*Radial distribution.* While B8 is masked by the SPHERE coronagraph, the inner ring in scattered light appears located inside B40 (see the middle panel of Figure 5), indicating that micron-sized grains are extending further in than the mm-sized grains. Such a spatial segregation by particle size is a natural outcome of dust trapping by a massive planet (Rice et al. 2006; Zhu et al. 2012; de Juan Ovelar et al. 2013; Pinilla et al. 2015b) and has already been observed in transition disks (e.g., Garufi et al. 2013). If the inner scattered-light ring traces the edge of the gap, it would be directly illuminated by the star and “puff up.” We propose that B40 lies in its shadow, which is

<sup>13</sup> We note that the SPHERE infrared ( $1.2 \mu\text{m}$ ) image has a resolution of  $37 \times 37$  mas, comparable to the spatial resolution of the ALMA observations (Benisty et al. 2018).

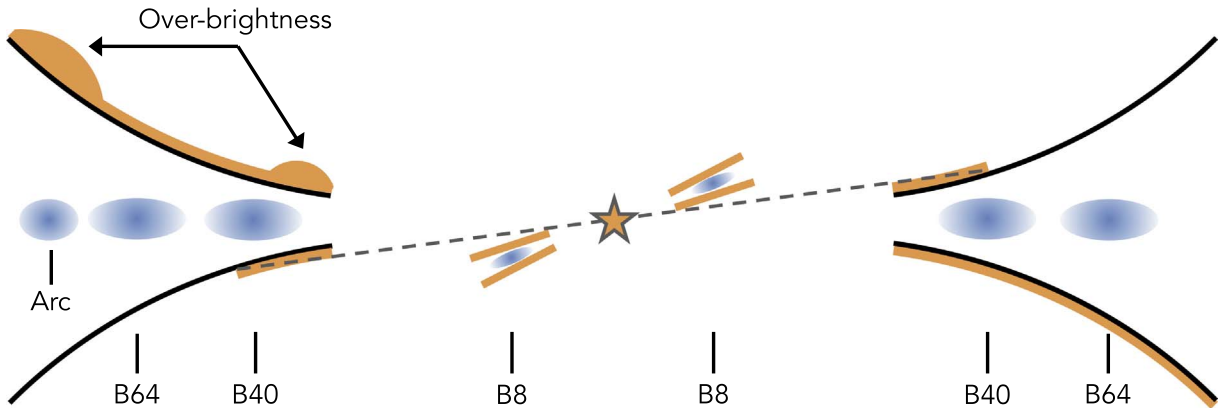


**Figure 6.** Schematics of the HD 143006 disk, comparing features traced by ALMA (detected rings/arc in color blue) and scattered-light SPHERE observations (illuminated surface in orange). The innermost ring detected by ALMA (namely B8) has an inner cavity and it is misaligned with respect to the outer disk, explaining the asymmetric illumination observed on the scattered-light images by Benisty et al. (2018), where one side of the disk is directly illuminated (top-left and bottom-right surface of the disk in the figure), while the other side is partially illuminated (inner top-right and bottom-left surface). A gap in scattered-light emission is observed inward of B40, while between B8 and B40 there is little millimeter emission observed. This is indicative of both small and large grains depletion the inner and outer disks. Two overbrightness are seen in scattered light, which line-up azimuthally with the arc seen at ALMA wavelengths. The outermost overbrightness appears radially collocated with the arc, while the innermost feature has no counterpart in the ALMA continuum image.

supported by a darker region seen just beyond the scattered-light inner ring (on the east side of the disk), and that the outer disk re-emerges from the shadow at a larger distance from the star (e.g., Dullemond & Dominik 2004; Isella & Turner 2018).

We note that a projected radial offset between the features seen in scattered light and in the millimeter could be expected due to the disk inclination and PA, the opening angle of the scattering surface, and the vertical structure of the ring (Dong et al. 2018). However, such an effect is considerable only for high disk inclinations. In that case, on the near side of the disk the scattered-light ring should appear inside B40, while on the far side, it should appear outside of it. That is not what we observe: the inner scattered-light ring is inside B40 at all PAs at which it is detected.

It is possible that a companion between B8 and B40 is shaping the disk, leading to the observed radial segregation and to a dust-depleted gap in both tracers of small and large dust grains. In this series, Zhang et al. (2018) constrain a planet mass of  $\sim 10\text{--}20 M_{\text{Jup}}$  based solely on the deep gap observed in ALMA images between B8 and B40. Such a high-mass companion is consistent with the hydrodynamic simulations coupled with dust evolution from de Juan Ovelar et al. (2013), which require a planet more massive than  $9M_{\text{Jup}}$  to be responsible for the observed radial segregation by particle size. Although we find a strong depletion in small grains that are well coupled to the gas, we do not detect clear depletion in CO emission between B8 and B40, suggesting that dust grains are filtered and that gas can still flow through the gap, similar to what is often seen in transition disks (Pinilla et al. 2015a).

*Azimuthal asymmetries.* The large east/west shadow (and the additional two narrow shadow lanes) observed in the SPHERE image can be explained by a moderate misalignment of  $\sim 20^\circ\text{--}30^\circ$  between the inner and outer disk (Benisty et al. 2018; see also the schematics in Figure 6). As shown in the residual map of Figure 4, B40 and B64 are symmetric, and we find no evidence for a counterpart of the east/west shadow in the continuum observations that would indicate inhomogeneities in the dust temperature. This supports the finding of Huang et al. (2018a), where the rings in HD 143006 are optically thin. Indeed, a configuration in which the inner and outer disks are moderately misaligned (see Figure 6) would lead to, for

example, the west side of the disk in the shadow while the east side is irradiated, for the front side of the disk that is facing us. On the backward-facing side of the disk (not seen by the observer) the opposite happens: the east side is in the shadow while the west is irradiated. If the disk is vertically optically thin, and the continuum emission traces the full vertical extent of the disk, the asymmetry will cancel out between the two sides, and the continuum emission would appear symmetric. We note, however, the presence of residuals (up to  $7\sigma$ ) in the south (PA  $\sim 180^\circ$ ) at the location where the east/west shadow starts. As in the CO data, there is no evidence for counterparts to the narrow shadow lanes in the continuum observations, unlike what is observed in two transition disks so far (DoAr 44, J1604; Casassus et al. 2018; Pinilla et al. 2018).

The bright arc in the ALMA image coincides with the overbrightness seen in the outer disk of the SPHERE image (see the contours in Figure 5 and the diagram in Figure 6). If the arc traces an overdensity in large grains, we also expect an enhancement of small particles due to fragmentation, and if turbulent mixing over the vertical height of the disk allows it, a small-particle enhancement should be seen from the surface layers as well. Additionally, the small grains seem to extend further, and over a wider range of PAs, than the larger particles, which is one of the predictions of dust trapping in a vortex (Baruteau & Zhu 2016). Future observations at shorter/longer ALMA wavelengths can test this idea by measuring the spread/concentration of particles over the arc location.

The inner ring from the scattered-light image shows a strong overbrightness that has no counterpart in the ALMA continuum image (see the contours inside B40 in Figure 5), and that is likely due to an irradiation effect and local change in scale height. Interestingly, it lies over a range of PAs that is similar to the one over which the arc extends in the ALMA continuum image. If the line-up is not coincidental, it must be related to a radiative effect, as any physical structure at such different radii would shear away the alignment quickly due to different angular rotation velocities. However, it is possible that the overbrightness along the first scattered-light ring further extends to the west (in the shadowed region), and that it covers a much broader range of PAs. In that case, the line-up could be coincidental.



In general, such differences likely mean that the small grains in the surface layers are only marginally affected by dynamical processes (while large grains in the midplane are), but are instead very much affected by irradiation processes.

#### 4.3. A Misalignment between the Inner and Outer Disks

Our continuum emission modeling indicates that the inner and outer disk do not share the same geometry, which is expected based on the shadows observed in the SPHERE image (Benisty et al. 2018). The inner disk appears inclined by  $24^\circ$  with a PA of  $164^\circ$ , while the outer disk has a lower inclination of  $17^\circ$  with a PA of  $176^\circ$ ; this difference in geometry is of high statistical significance (see Table 2). Based on these values, we can estimate the misalignment angle between the inner and outer disks, defined as the angle between the normal vectors to the disks. Assuming the values above, we find a small misalignment of  $8^\circ$ . However, this assumes that the inner and outer disks share the same near side of the disk (the side closer to us), which cannot be determined with the continuum data alone. If instead the near sides do not coincide (e.g., the near side of the outer disk is in the east, while the near side of the inner disk is in the west), then the misalignment would be much larger ( $41^\circ$ , computed using  $i = -24^\circ$  for the inner disk, the rest of the parameters being the same as above). In this case, once projected onto the plane of the sky, the inner disk rotation would appear as counter-rotating with respect to the outer disk. This is not something seen in the CO data (at an angular resolution of  $66 \times 49$  mas,  $\sim 9$  au), in particular at the highest velocities. Nevertheless, the fit of the intensity-weighted velocity map with a Keplerian disk model shows residuals inside  $0''.15$ , supporting a different geometry than the one of the outer disk.

The location of the shadows seen in scattered light depend on the inner and outer disk geometry, and on the height of the scattering surface ( $z_{\text{scat}}$ ) of the disk where the shadows are seen. Using the equations developed in Min et al. (2017), we find a  $z_{\text{scat}}/R$  of  $\sim 0.03$  and  $\sim 0.16$  at  $\sim 18$  au (the location of the inner scattered-light ring), for misalignment angles of  $7^\circ$  and  $41^\circ$ , respectively. The pressure scale height of the disk,  $H_p$ , should be smaller than the scattering surface (by a factor of  $\sim 2$ – $4$ ), therefore we expect  $H_p/R < 0.015$  and  $< 0.08$  at  $\sim 18$  au, for misalignment angles of  $7^\circ$  and  $41^\circ$ , respectively. From the standard temperature profile assumed in Huang et al. (2018a), we estimate that at 18 au  $H_p/R \sim 0.04$ . Given the small  $H_p/R$  expected for a  $7^\circ$  misalignment and the larger value of the pressure scale height as estimated above from standard assumptions, we favor the larger misalignment value of  $41^\circ$ .

The overall morphology of the shadows in the scattered-light image were reproduced by a circumbinary disk that is broken and misaligned by  $\sim 30^\circ$  (Benisty et al. 2018), due to an inclined equal-mass binary (see the hydrodynamical simulations by Facchini et al. 2018). We note, however, that the value of the misalignment needed to reproduce the scattered-light image is model dependent, and depends on the exact geometry of the inner disk as well as on the shape of the outer disk rim considered in the model.

The presence of an equal-mass binary companion, as well as of any companion with a mass ratio larger than  $q = 0.2$  (corresponding to  $0.3 M_\odot$ ), can be ruled out as it would have been detected by imaging and interferometric surveys (Kraus et al. 2008; Benisty et al. 2018). However, an inclined low-mass stellar companion, as the one detected in the wide gap of

HD 142527 (with a mass  $\sim 0.13 M_\odot$ ), could be responsible for the misalignment (Price et al. 2018), and secular precession resonances can result in large misalignments for companions with mass ratio of 0.01–0.1 (Owen & Lai 2017). A massive planet could in principle also lead to a misaligned inner disk as long as its angular momentum is larger than that of the inner disk (e.g., Bitsch et al. 2013; Xiang-Grüss & Papaloizou 2013; Matsakos & Königl 2017), i.e., in cases where the inner disk is depleted.

In any case, it is not clear whether or not the putative companion responsible for the misalignment in HD 143006 should be located in the gap between B8 and B40, or between B8 and the dust sublimation edge. The spectral energy distribution indicates the presence of hot dust close to the sublimation radius, which was spatially resolved by near-infrared interferometry (Lazareff et al. 2017), suggestive of the presence of (at least) another ring of small dust in the innermost au where mm-sized grains are depleted.

## 5. Conclusions

From the DSHARP ALMA observations of the HD 143006 protoplanetary disk that reach  $\sim 7$  au in spatial resolution, and its comparison with existing scattered-light observations at similar spatial resolution, we conclude the following.

1. In terms of substructure, the dust continuum emission from HD 143006 reveals three bright rings, two dark gaps, and an arc at the edge of the dusty disk. The CO observations at similar angular resolution exhibit a depletion of gas emission in the inner disk with no significant features, except for a deviation or “kink” from the Keplerian rotation pattern over a few redshifted channels close to the systemic velocity.
2. From different tracers of the disk structure we find further evidence for a misalignment between the inner and outer disk: a fit to the disk Keplerian velocities with a global/single disk geometry does not account well for the inner disk kinematics, while modeling of dust continuum emission results in a more inclined inner disk (as traced by B8) than the outer disk (as traced by B40, B64, and the southeast arc). These findings are in agreement with existing VLT/SPHERE images that suggest a disk misalignment from the presence of shadows.
3. The prominent southeast arc in the ALMA 1.25 mm image resolves into three peaks along its azimuthal extent. The counterpart to this arc in the scattered-light image shows a broader radial and azimuthal extent, indicative of segregation by particle size as would be expected for a dust-trapping vortex at this location. Future observations at longer wavelengths should be able to test this scenario.
4. The bright rings have increasingly larger radial widths with increasing distance from the star. We find evidence for radial segregation by particle size at the outer edge of the gap between B8 and B40, and a strong depletion of small and large grains in the gap. These are consistent with a companion carving the gap. However, no dark annulus is observed in CO emission at this radius, suggesting that dust grains are filtered but gas can still flow through the gap.

Future observations at longer millimeter wavelengths will allow us to determine if there is efficient trapping of dust at the

substructure's location, if these are due to localized pressure maxima, and in particular to understand if the arc traces a vortex. Observing gas tracers at high spectral resolution will also be fundamental for elucidating the absolute misalignment of the inner disk and determining the velocity structure at the arc location.

We are thankful to S. Facchini, A. Juhász, and R. Teague for insightful discussions. This Letter makes use of ALMA data [ADS/JAO.ALMA#2016.1.00484.L](#) and [ADS/JAO.ALMA#2015.1.00964.S](#)). ALMA is a partnership of ESO (representing its member states), NSF (USA) and NINS (Japan), together with NRC (Canada), MOST and ASIAA (Taiwan), and KASI (Republic of Korea), in cooperation with the Republic of Chile. The Joint ALMA Observatory is operated by ESO, AUI/NRAO and NAOJ. L.P. acknowledges support from CONICYT project Basal AFB-170002, from FCFM/U. de Chile Fondo de Instalación Académica, and from FONDECYT Iniciación project #11181068. M.B. acknowledges funding from ANR of France under contract No. ANR-16-CE31-0013 (Planet Forming disks). S.A. and J.H. acknowledge funding support from NASA Exoplanets Research Program grant 80NSSC18K0438. T.B. acknowledges funding from the European Research Council (ERC) under the European Unions Horizon 2020 research and innovation programme under grant agreement No. 714769. C.P.D. acknowledges support by the German Science Foundation (DFG) Research Unit FOR 2634, grants DU 414/22-1 and DU 414/23-1. V.V.G. and J.C acknowledge support from the National Aeronautics and Space Administration under grant No. 15XRP15\_20140 issued through the Exoplanets Research

Program. J.H. acknowledges support from the National Science Foundation Graduate Research Fellowship under grant No. DGE-1144152. A.I. acknowledges support from the National Aeronautics and Space Administration under grant No. NNX15AB06G issued through the Origins of Solar Systems program, and from the National Science Foundation under grant No. AST-1715719. L.R. acknowledges support from the ngVLA Community Studies program, coordinated by the National Radio Astronomy Observatory, which is a facility of the National Science Foundation operated under cooperative agreement by Associated Universities, Inc. Z.Z. and S.Z. acknowledge support from the National Aeronautics and Space Administration through the Astrophysics Theory Program with grant No. NNX17AK40G and Sloan Research Fellowship. Simulations are carried out with the support from the Texas Advanced Computing Center (TACC) at The University of Texas at Austin through XSEDE grant TG-AST130002.

### Appendix Additional Figures

Here we present additional supporting figures. First, a zoom-in to the channel maps near the systemic velocity that show a “kink” on the redshifted channels (bottom panels of Figure 7) that is not present on the blueshifted channels (top panels of Figure 7). Second, Figure 8 shows how the Keplerian velocity fit differs when the intensity-weighted velocity field map has been masked inside  $0''.15$  (top panels, Figure 8) and masked outside of  $0''.15$  (bottom panels, Figure 8).

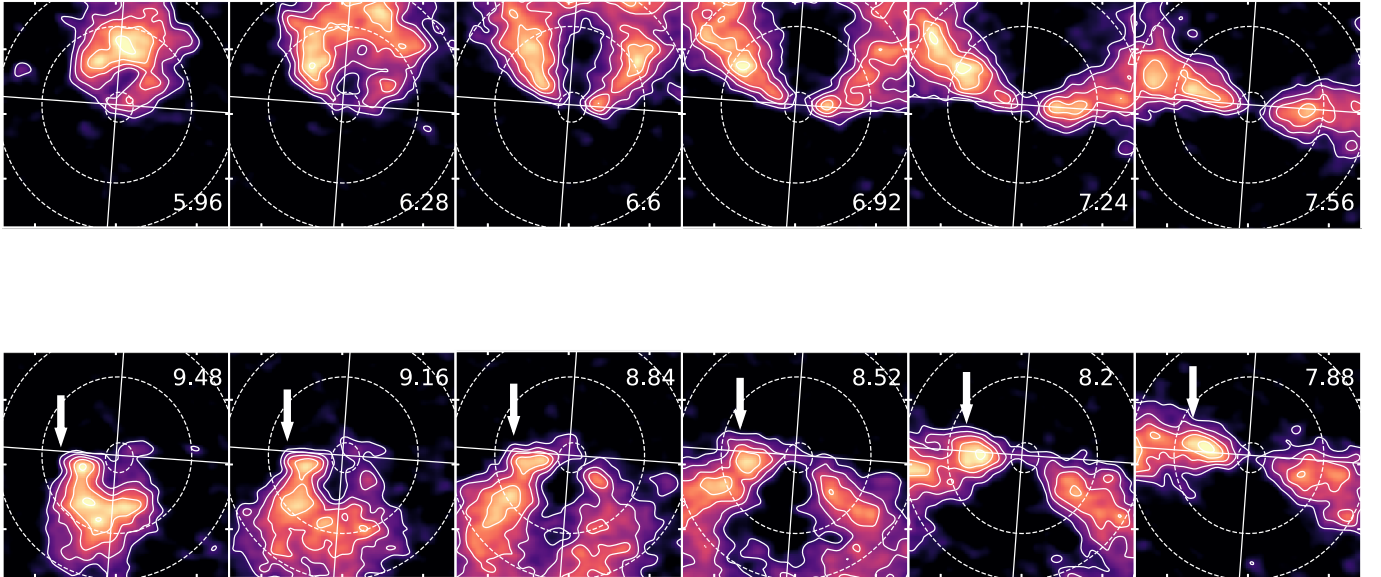


**Figure 7.** Zoom-in to the channel maps near the systemic velocity of HD 143006, with blueshifted and redshifted channels on the top and bottom, respectively. Note that the redshifted channel ordering has been flipped (velocity increasing toward the left) to aid the comparison with its symmetric channels on the blueshifted side of the line. The arrow marks the perturbation or “kink” seen at similar PA as the bright overdensity in scattered light. Notice also how different the emission is in the region marked by the arrow compared to the symmetric channel on the top.

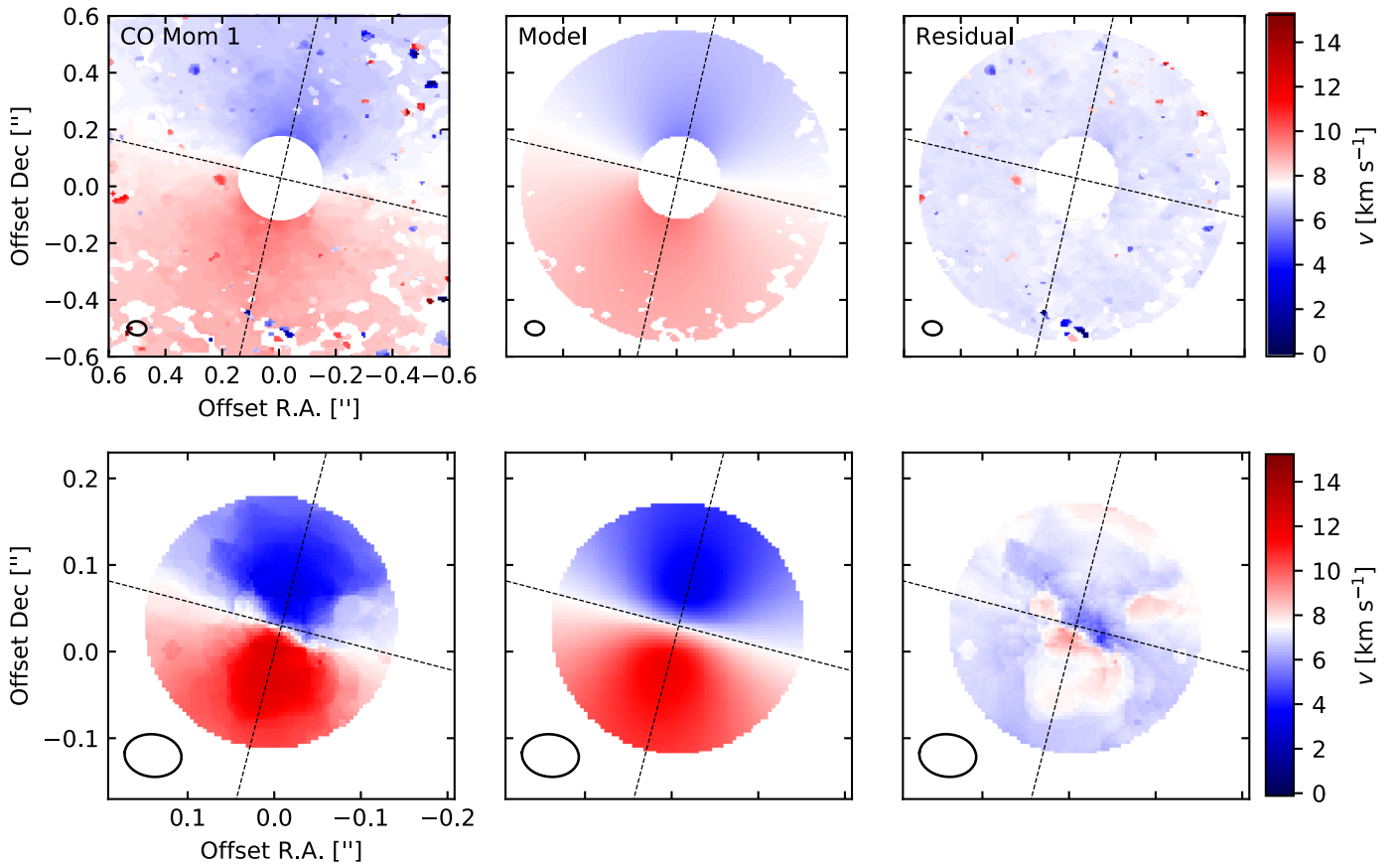


**Figure 8.** Comparison between the intensity-weighted velocity field around HD 143006 (right panels), the best-fit model for a Keplerian razor-thin disk (middle panels), and the residual velocity field map obtained from subtracting the best-fit model from the observations (left panels). The top panels show the fit results when the inner disk is masked (inside of  $0.15''$ ), while the bottom panels have been zoomed in and show the fit results when the outer disk is masked (outside of  $0.15''$ ). The PA of the disk that is obtained from each fit ( $167.0^\circ$  for the top panels,  $165.6^\circ$  for the bottom panels), are indicated by dashed lines.

### ORCID iDs

Laura M. Pérez <https://orcid.org/0000-0002-1199-9564>  
 Myriam Benisty <https://orcid.org/0000-0002-7695-7605>  
 Sean M. Andrews <https://orcid.org/0000-0003-2253-2270>  
 Andrea Isella <https://orcid.org/0000-0001-8061-2207>  
 Cornelis P. Dullemond <https://orcid.org/0000-0002-7078-5910>  
 Jane Huang <https://orcid.org/0000-0001-6947-6072>  
 Zhaohuan Zhu <https://orcid.org/0000-0003-3616-6822>  
 Tilman Birnstiel <https://orcid.org/0000-0002-1899-8783>  
 Shangjia Zhang <https://orcid.org/0000-0002-8537-9114>  
 John M. Carpenter <https://orcid.org/0000-0003-2251-0602>  
 David J. Wilner <https://orcid.org/0000-0003-1526-7587>  
 Xue-Ning Bai <https://orcid.org/0000-0001-6906-9549>  
 Karin I. Öberg <https://orcid.org/0000-0001-8798-1347>

### References

- ALMA Partnership, Brogan, C. L., Pérez, L. M., et al. 2015, *ApJL*, **808**, L3  
 Andrews, S., Huang, J., Pérez, L. M., et al. 2018, *ApJL*, **869**, L41  
 Ataiee, S., Pinilla, P., Zsom, A., et al. 2013, *A&A*, **553**, L3  
 Avenhaus, H., Quanz, S. P., Garufi, A., et al. 2018, *ApJ*, **863**, 44  
 Avenhaus, H., Quanz, S. P., Schmid, H. M., et al. 2014, *ApJ*, **781**, 87  
 Bai, X.-N., & Stone, J. M. 2014, *ApJ*, **796**, 31  
 Barenfeld, S. A., Carpenter, J. M., Ricci, L., et al. 2016, *ApJ*, **827**, 142  
 Barge, P., & Sommeria, J. 1995, *A&A*, **295**, L1  
 Baruteau, C., & Zhu, Z. 2016, *MNRAS*, **458**, 3927  
 Benisty, M., Stolker, T., Pohl, A., et al. 2017, *A&A*, **597**, A42  
 Benisty, M., Juhász, A., Facchini, S., et al. 2018, *A&A*, **619**, A171  
 Béthune, W., Lesur, G., & Ferreira, J. 2017, *A&A*, **600**, A75  
 Birnstiel, T., Dullemond, C. P., & Brauer, F. 2010, *A&A*, **513**, A79  
 Birnstiel, T., Dullemond, C. P., & Pinilla, P. 2013, *A&A*, **550**, L8  
 Bitsch, B., Crida, A., Libert, A.-S., et al. 2013, *A&A*, **555**, A124  
 Bouvier, J., Alencar, S. H. P., Bouvier, T., et al. 2007, *A&A*, **463**, 1017  
 Brauer, F., Dullemond, C. P., Johansen, A., et al. 2007, *A&A*, **469**, 1169  
 Casassus, S., Avenhaus, H., Pérez, S., et al. 2018, *MNRAS*, **477**, 5104  
 Casassus, S., Marino, S., Pérez, S., et al. 2015, *ApJ*, **811**, 92  
 Casassus, S., van der Plas, G. M., Perez, M. A., et al. 2013, *Natur*, **493**, 191  
 Cazzoletti, P., van Dishoeck, E. F., Pinilla, P., et al. 2018, *A&A*, **619**, A161  
 Cody, A. M., Stauffer, J., Baglin, A., et al. 2014, *AJ*, **147**, 82  
 Crida, A., & Morbidelli, A. 2007, *MNRAS*, **377**, 1324  
 de Juan Ovelar, M., Min, M., Dominik, C., et al. 2013, *A&A*, **560**, A111  
 Dittrich, K., Klahr, H., & Johansen, A. 2013, *ApJ*, **763**, 117  
 Dong, R., Liu, S.-Y., Eisner, J., et al. 2018, *ApJ*, **860**, 124  
 Dullemond, C. P., Birnstiel, T., Huang, J., et al. 2018, *ApJL*, **869**, L46  
 Dullemond, C. P., & Dominik, C. 2004, *A&A*, **417**, 159  
 Facchini, S., Juhász, A., & Lodato, G. 2018, *MNRAS*, **473**, 4459  
 Flock, M., Fromang, S., Turner, N. J., et al. 2017, *ApJ*, **835**, 230  
 Foreman-Mackey, D., Hogg, D. W., Lang, D., & Goodman, J. 2013, *PASP*, **125**, 306  
 Fu, W., Li, H., Lubow, S., Li, S., & Liang, E. 2014, *ApJL*, **795**, L39  
 Gaia Collaboration, Brown, A. G. A., Vallenari, A., et al. 2018, *A&A*, **616**, A1  
 Garufi, A., Benisty, M., Pinilla, P., et al. 2018, *A&A*, **620**, A94  
 Garufi, A., Quanz, S. P., Avenhaus, H., et al. 2013, *A&A*, **560**, A105  
 Huang, J., Andrews, S. M., Dullemond, C. P., et al. 2018, *ApJL*, **869**, L42  
 Huang, J., Andrews, S. M., Pérez, L. M., et al. 2018, *ApJL*, **869**, L43  
 Isella, A., Huang, J., Andrews, S. M., et al. 2018, *ApJL*, **869**, L49  
 Isella, A., Pérez, L. M., Carpenter, J. M., et al. 2013, *ApJ*, **775**, 30  
 Isella, A., & Turner, N. J. 2018, *ApJ*, **860**, 27  
 Johansen, A., Youdin, A., & Klahr, H. 2009, *ApJ*, **697**, 1269  
 Klahr, H., & Henning, T. 1997, *Icar*, **128**, 213  
 Kraus, A. L., Ireland, M. J., Martinache, F., et al. 2008, *ApJ*, **679**, 762  
 Kretke, K. A., & Lin, D. N. C. 2007, *ApJL*, **664**, L55



- Lazareff, B., Berger, J.-P., Kluska, J., et al. 2017, [A&A](#), **599**, A85
- Li, H., Finn, J. M., Lovelace, R. V. E., et al. 2000, [ApJ](#), **533**, 1023
- Lobo Gomes, A., Klahr, H., Uribe, A. L., et al. 2015, [ApJ](#), **810**, 94
- Loomis, R. A., Öberg, K. I., Andrews, S. M., et al. 2017, [ApJ](#), **840**, 23
- Lyra, W., & Lin, M.-K. 2013, [ApJ](#), **775**, 17
- Marino, S., Perez, S., & Casassus, S. 2015, [ApJL](#), **798**, L44
- Matsakos, T., & Königl, A. 2017, [AJ](#), **153**, 60
- Meheut, H., Meliani, Z., Varniere, P., et al. 2012, [A&A](#), **545**, A134
- Min, M., Stolker, T., Dominik, C., et al. 2017, [A&A](#), **604**, L10
- Okuzumi, S., Momose, M., Sirono, S.-I., et al. 2016, [ApJ](#), **821**, 82
- Owen, J. E., & Lai, D. 2017, [MNRAS](#), **469**, 2834
- Paardekooper, S.-J., & Mellema, G. 2004, [A&A](#), **425**, L9
- Pecaut, M. J., Mamajek, E. E., & Bubar, E. J. 2012, [ApJ](#), **746**, 154
- Pérez, L. M., Isella, A., Carpenter, J. M., & Chandler, C. J. 2014, [ApJL](#), **783**, L13
- Perez, S., Dunhill, A., Casassus, S., et al. 2015, [ApJL](#), **811**, L5
- Pinilla, P., Benisty, M., & Birnstiel, T. 2012a, [A&A](#), **545**, A81
- Pinilla, P., Benisty, M., de Boer, J., et al. 2018, [ApJ](#), **868**, 85
- Pinilla, P., Birnstiel, T., Ricci, L., et al. 2012b, [A&A](#), **538**, A114
- Pinilla, P., de Boer, J., Benisty, M., et al. 2015a, [A&A](#), **584**, L4
- Pinilla, P., de Juan Ovelar, M., Ataiee, S., et al. 2015b, [A&A](#), **573**, A9
- Pinte, C., Price, D. J., Ménard, F., et al. 2018, [ApJL](#), **860**, L13
- Preibisch, T., Brown, A. G. A., Bridges, T., Guenther, E., & Zinnecker, H. 2002, [AJ](#), **124**, 404
- Price, D. J., Cuello, N., Pinte, C., et al. 2018, [MNRAS](#), **477**, 1270
- Regály, Z., Juhász, A., & Nehéz, D. 2017, [ApJ](#), **851**, 89
- Regály, Z., Juhász, A., Sándor, Z., et al. 2012, [MNRAS](#), **419**, 1701
- Rice, W. K. M., Armitage, P. J., Wood, K., et al. 2006, [MNRAS](#), **373**, 1619
- Rigliaco, E., Pascucci, I., Duchene, G., et al. 2015, [ApJ](#), **801**, 31
- Rosenfeld, K. A., Andrews, S. M., Hughes, A. M., Wilner, D. J., & Qi, C. 2013, [ApJ](#), **774**, 16
- Rosenfeld, K. A., Chiang, E., & Andrews, S. M. 2014, [ApJ](#), **782**, 62
- Rosenfeld, K. A., Qi, C., Andrews, S. M., et al. 2012, [ApJ](#), **757**, 129
- Simon, J. B., & Armitage, P. J. 2014, [ApJ](#), **784**, 15
- Stolker, T., Dominik, C., Avenhaus, H., et al. 2016, [A&A](#), **595**, A113
- Suriano, S. S., Li, Z.-Y., Krasnopolsky, R., & Shang, H. 2018, [MNRAS](#), **477**, 1239
- Tazzari, M., Beaujean, F., & Testi, L. 2018, [MNRAS](#), **476**, 4527
- Teague, R., Bae, J., Bergin, E. A., et al. 2018, [ApJL](#), **860**, L12
- van der Marel, N., van Dishoeck, E. F., Bruderer, S., Pérez, L., & Isella, A. 2015, [A&A](#), **579**, A106
- Walsh, C., Daley, C., Facchini, S., et al. 2017, [A&A](#), **607**, A114
- Weaver, E., Isella, A., & Boehler, Y. 2018, [ApJ](#), **853**, 113
- Xiang-Gruess, M., & Papaloizou, J. C. B. 2013, [MNRAS](#), **431**, 1320
- Zhang, K., Blake, G. A., & Bergin, E. A. 2015, [ApJL](#), **806**, L7
- Zhang, S., et al. 2018, [ApJ](#), submitted
- Zhu, Z., & Baruteau, C. 2016, [MNRAS](#), **458**, 3918
- Zhu, Z., Nelson, R. P., Dong, R., Espaillat, C., & Hartmann, L. 2012, [ApJ](#), **755**, 6
- Zhu, Z., Nelson, R. P., Hartmann, L., et al. 2011, [ApJ](#), **729**, 47
- Zhu, Z., & Stone, J. M. 2014, [ApJ](#), **795**, 53